electronics

MDPI

Article

An Array-Type System Applied to Complex Surfaces in Nuclear Pollution Detection

Hongyu Chu [1,*], Zhiyuan Chang [1], Yanhua Shao [1], Xiaoqiang Zhang [1] and Jaime Lloret [2,3,*]

[1] School of Information Engineering, Southwest University of Science and Technology, Mianyang 621010, China; changzy89@gmail.com (Z.C.); syh@cqu.edu.cn (Y.S.); xqzhang@swust.edu.cn (X.Z.)
[2] Instituto de Investigacion para la Gestion Integrada de Zonas Costeras (IGIC), Universitat Politecnica de Valencia, 46022 Valencia, Spain
[3] School of Computing and Digital Technologies, Staffordshire University, Stoke ST4 2DE, UK
* Correspondence: chuhongyu@swust.edu.cn (H.C.); jlloret@dcom.upv.es (J.L.)

Received: 23 August 2020; Accepted: 4 November 2020; Published: 6 November 2020

Abstract: Radioactive pollution detection plays a key role in nuclear technology application. In this paper, an array-type of nuclear pollution detection system is designed for the detection scenario of complex surfaces. Firstly, to get the three-dimensional point cloud of the surface, a complex surface was modeled based on the geometric ranging model of a two-dimensional laser profilometer and the motion model of a two-degree-of-freedom displacement platform. Secondly, an 'S' type scanning scheme of profilometer was developed to overcome the problem of limited scanning area of the profilometer. Thirdly, Euclidean distance weighted median filtering was used to solve the impulsive noise that may occur during the point cloud acquisition process. Finally, the 3D point cloud information of the complex surface was used for controlling the movement of the 6×6 array channel pollution detector to complete the α and β particle measurement tasks. A mechanical platform was constructed for experiments, the results are as follows. The working range of this system is from -5 cm to 5 cm in elevation difference of surfaces, and the accuracy is 12 μm in surface height measuring. It takes 26.13 s to perform a detection task including surface scanning and the detector moving, and scanning accuracy is 0.35×0.35 mm^2. The maximum control error of the surface contamination detector is 0.4 mm. Specifically, the detection area of the system reaches 240×240 mm^2. The results show that the system acquires three-dimensional terrain information, and realizes control over the movement of the pollution detector accurately and then completes the detection of α and β particles effectively.

Keywords: nuclear pollution detection; laser profilometer; three-dimensional point cloud; point cloud registration; weighted median filter

1. Introduction

In recent years, the extensive application of nuclear technology has brought a lot of convenience to human survival, but some potential harm to the natural environment that has also attracted the attention of the international community. Radioactive radiation has been listed as one of the main public hazards by the United Nations Conference on Human Environmental Protection (UNCHEP) [1–4]. Radioactive pollution monitoring technology is an important part of nuclear technology. In the monitoring process, α and β particles are especially targeted due to such characteristics as weak penetration and strong ionization. These are devastating abilities that may destroy body tissues to seriously threaten human health [5]. This is why nuclear safety supervision should always be strictly implemented so as to minimize this sort of adverse effect. It is of great significance to detect α and β particles quickly and accurately on the surface of an object and the surrounding environment.

The traditional detection for nuclear pollution methods mainly include manual hand-held detection, mobile robot for detection and flying robot for detection. The manual detection [6–9] method has the characteristics of strong environmental adaptability and high precision, but it has high requirements for the staff, and it is difficult to keep the distance between the detector and each detection point consistent. Mobile robots [10–12] equipped with detector for detection of nuclear pollution require lower requirements for the staff. Comparing with manual detection, the efficiency is greatly improved. But the complex surface environment will limit the movement of mobile robots, and it is difficult to complete the task of detecting. Flying robots [13–19] equipped with detector are mainly used for nuclear pollution detection in the air, with a wide detection range, but there are problems such as low detection accuracy for detection of complex surfaces.

Aiming at the problems of the above detection methods in nuclear pollution detection applied to complex surfaces, an array-type of nuclear pollution detection system is designed. Firstly, the system adopts a two-dimensional laser profilometer to get three-dimensional point cloud of the surface, then controls the movement of the 6×6 array channel pollution detector to complete the α and β particle measurement tasks based on three-dimensional point cloud. Finally, a mechanical platform was constructed for experiments, the results show that the system completes the detection of α and β particles effectively.

The rest of the paper is organized as follows: In Section 2, there is an overview presentation on related work. In Section 3, a nuclear contamination detection scheme is introduced for the complex surfaces, including measurement methods for complex topographic surfaces, surface contamination detector with motion control strategies, and array detection units for surface contamination. In Section 4, the implementation of the system is elaborated, and three experiments are performed to verify the effectiveness and feasibility of the system. Experimental results show that the system provides a feasible method for nuclear contamination detection of complex surfaces to obtain three-dimensional information. In Section 5, the performance of the proposed method is evaluated and discussed. In Section 6, some work summary and conclusions for the proposed method are presented.

2. Related Work

In this section, we briefly summarize different types of nuclear pollution detection methods, including manual hand-held detection, mobile robot for detection and flying robot for detection.

2.1. Manual Detection

A PRD (personal radiation detector) can detect the dose equivalent rate at the position of the wearer [6]. An alpha/beta surface contamination monitor are mainly used to measure the surface of goods on site whether there are radioactive substances and intensity. Low background alpha and beta measuring instruments are used for accurately measuring activity in a sample in laboratory tests usually. This handheld method is flexible in scheduling, but the action is slow and range is small. To do this, personnel need to participate in a close position. The biggest trouble is the difficulty of the control over the distance between the detector and the target surface [7–9].

2.2. Mobile Robot

Comparing with the handheld operation, the nuclear pollution detection task is changed from manual mode to automatic mode. With good maneuverability, the mobile robot gets more efficient information in checking the measurement area [10,11]. For instance, the Ducros [12] team developed a RICA (Robot d' Inspection pour Cellules Aveugles) mobile robot for radioactive source positioning and measurement. A spectrometer, along with the α and β particles measurement detectors, it can execute nuclear source detection tasks in a radiation environment.

2.3. Flying Robot

With the development of UAV (unmanned aerial vehicle) technology, UAVs are gradually used in nuclear radiation detection tasks [13–18]. In spite of its unparalleled advantages of detection speed, maneuverability, and detection range, this kind of new tool may be held back in detecting the air environment, being unable to take on the job to accurately measure the surface α and β particles. For example, the G. Micconi et al. [19] developed a remotely-piloted aerial system (RPAS) for environmental monitoring. The system is specifically used to detect radiant substances in outdoor environments. RPAS includes a drone platform, a light radiation detector and a set of HMI (human machine interface) system as well as a remote operation interface designed for environmental monitoring.

3. Nuclear Pollution Detection Scheme for Complex Surfaces

The method proposed in this paper mainly includes three parts, surface topography measurement method, motion control strategy of surface pollution detector, and the human-computer interface. The program block diagram is shown in Figure 1.

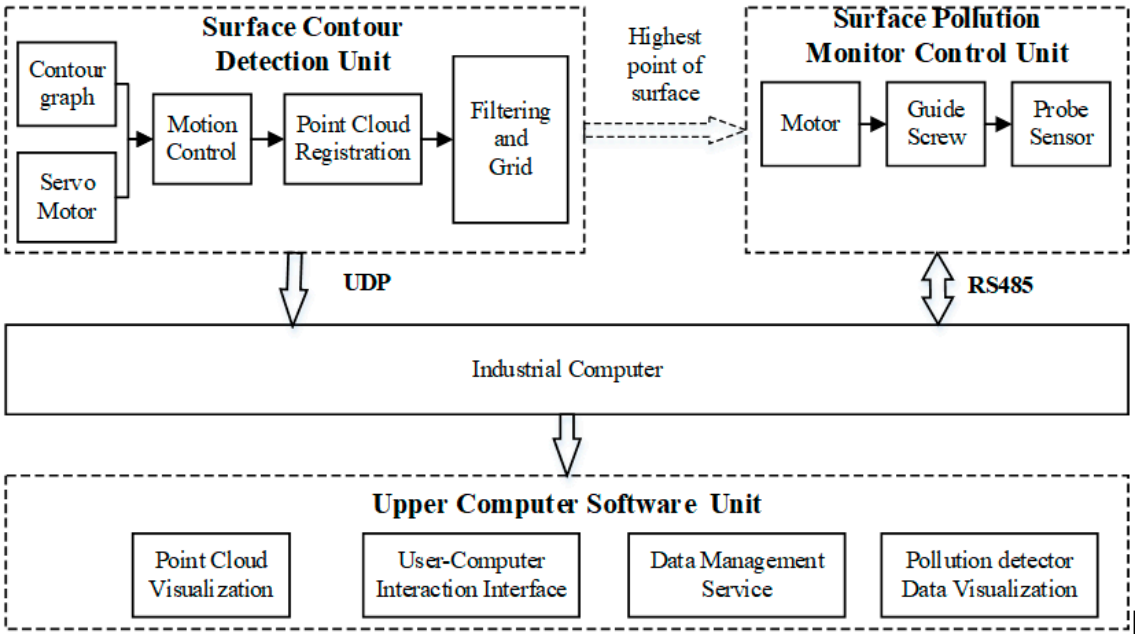

Figure 1. Block diagram of nuclear pollution detection scheme.

Firstly, the geometric distance measurement model and the motion model of the profilometer were placed to sample the surface of the point cloud by utilizing the 2D laser profilometer. Through coordinate transformation, the point cloud data was then registered to obtain a complete 3D Point cloud. Subsequently, the point cloud data was smoothened based on weighted median filtering of Euclidean distance. Then building 6 × 6 channel detectors on the measured surface for projection, and rasterize the point cloud into 6 × 6 small equal area blocks to map each detection channel separately, followed by calculating the maximum value of the point cloud corresponding to each measurement channel. The horizontal initial position information of the detector was integrated to calculate the input of the motor. An encoder was set up to record the motor movement count to achieve closed-loop control of the pollution detector movement. Finally, after the surface contamination detector moved to the desired position, a special unit started to detect the activity of α and β particles, and the data were transmitted to the host computer for data visualization and storage.

3.1. Measurement of Complex Surface Topography

Limited by factors such as light, material, equipment installation control and cost, the commonly used 3D information measurement method for large area is not suitable for this application. Thanks to its high precision and less sensitiveness to light, a two-dimensional laser profilometer was chosen for surface topography measurement.

There two-dimensional laser profilometer was only to obtain the *X*-axis and *Z*-axis elevation information of the terrain, not prepared to determine the *Y*-axis coordinate information of the terrain. Therefore, it is necessary to obtain the three-dimensional data of the terrain by controlling the movement of the equipment and integrating the motion posture information. The complex surface topography measurement goes through surface topography 3D modeling, point cloud registration and point cloud filtering. The block diagram of the topographic measurement process is shown in Figure 2.

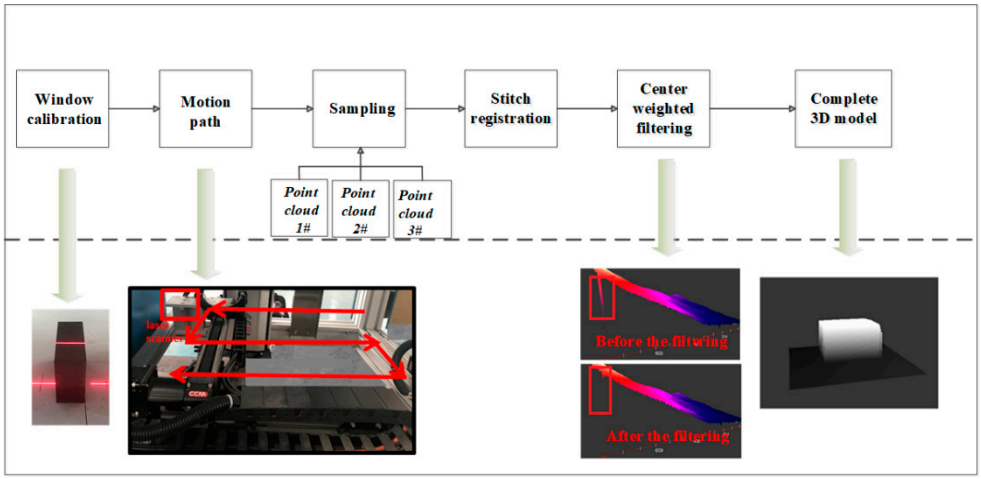

Figure 2. Block diagram of topographic survey process.

Cell Calibration was used to establish the positional relationship between the coordinate system of the profilometer and the measurement cell. As per the calibration parameters of the measurement window, the motion control strategy of the profilometer and the registration of point cloud data were designed. The impulse noise was then eliminated by the Euclidean distance weighted median filter, and finally the complete three-dimensional information of the surface was obtained.

3.1.1. Three-Dimensional Modeling of Complex Terrain Surface

A two-dimensional laser profilometer was used to model the surface terrain with the help of a two-degree-of-freedom displacement platform motion. This makes sure that the three-dimensional information of the surface be recovered quickly and accurately. First, the geometric distance measurement model of the two-dimensional laser profilometer was analyzed. In the limited measurement range, the laser profilometer was unable to cover the entire measured surface at once. Therefore, an 'S' type scanning scheme was developed to make up for the shortcomings of the equipment range, i.e., detecting the target area in blocks. This 'S' type motion parameter was connected with two factors: the geometric model of the single measurement of the profilometer and the position coordinates of the window calibration. The single measurement model of the laser profilometer is shown in Figure 3.

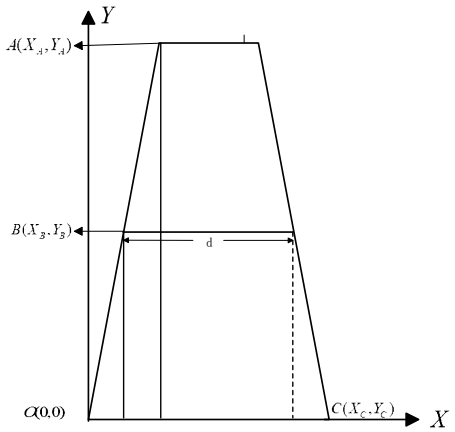

Figure 3. Geometric model of laper profilometer from single measurement.

The effective measurement area of the profilometer is distributed in the shape of a trapezoid. In the measurement area of the profilometer, the bottom edge of the trapezoid is the *X*-axis. The *X*-axis intersects the vertical line Y at O as the origin to establish a two-dimensional plane coordinate system, where Point A is the end point of the upper base of the trapezoid, Point B is the point on the waist of the trapezoid, and Point C is the end point of the lower base of the trapezoid. In the extreme case, the highest point of the target surface does not exceed Point B, to avoid the height of the surface from overflowing the effective measuring range of the profilometer. The single scanning width of the profilometer cannot exceed d. The position of Points A, O and C may be fixed by the way of window calibration, and the effective scanning width *d* of the profilometer is calculated as:

$$d = X_C - 2(\frac{X_A Y_B}{Y_A}) \quad (1)$$

To overcome the range defect of a single device, a profilometer motion path planning was designed in line with the above laser profilometer measurement model and window calibration parameters. Thus, the measurement of all three-dimensional information of the regional terrain was completed. The device movement path is shown in Figure 4.

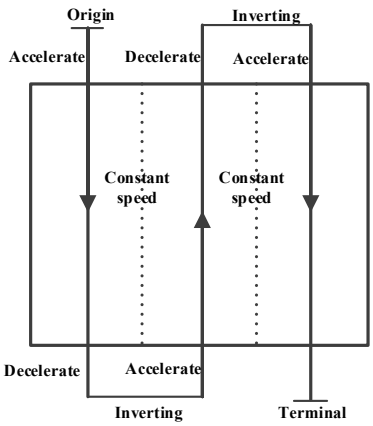

Figure 4. Schematic diagram of movement path of profilometer.

The profilometer works along an 'S' type scanning mode. The motion process from the start point to the end point includes four motion modes of acceleration, uniform speed, deceleration, and commutation. During the sampling period, the motion is maintained at a uniform speed by adopted the acceleration/deceleration control algorithm based on trapezoid-curve, so that a regular three-dimensional point cloud image can be obtained to reduce the difficulty and runtime of subsequent

point cloud registration. A point cloud image is a digital point set measured by a scanning device on a solid model. Each point in the point set contains its physical information. The profilometer only obtains one-dimensional position and depth information. The 'S' type scanning mode, combined with laser profilometer ranging model, quickly and accurately may obtain a three-dimensional point cloud. A world coordinate system was established with the upper left corner of the measurement window as the coordinate origin. In the trapezoidal area measured by the profilometer, the center line of the bottom edge was taken as the carrier coordinate system, as shown in Figure 5.

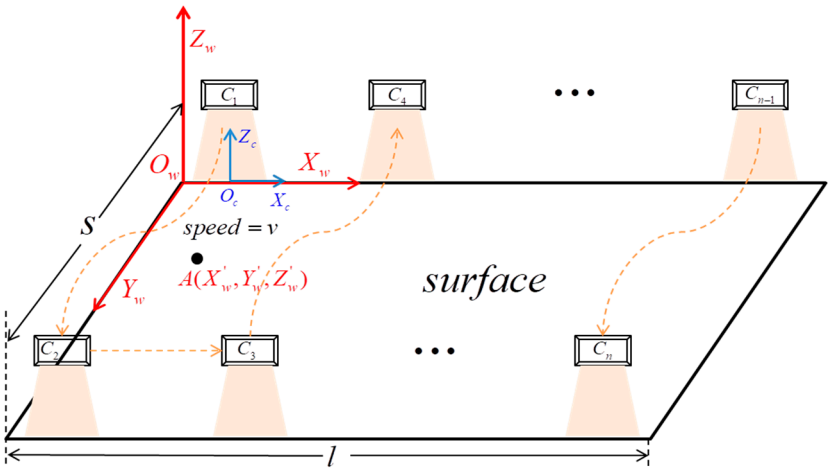

Figure 5. Coordinate system of profilometer carrier and world coordinate system of measuring area.

In the measurement window, establish a world coordinate system.$O_w - X_w Y_w Z_w$, carrier coordinate system $O_c - X_c Z_c$, make the X_w axis in the carrier coordinate system parallel to the X_w axis in the world coordinate system, and control the laser profilometer on Y_w the shaft moves at a constant speed. Nevertheless, there is an acceleration and deceleration process in the movement of the laser profilometer. Therefore, before the X_c axis of the carrier coordinate system coincided with the X_w axis of the world coordinate system, the profilometer must move at a constant speed to ensure that the coordinate system of the terrain world Y_w on the axis was evenly sampled, and the 3D model recovered later would not be distorted. Set the measured plane length to s, the profilometer scan frequency to f, and the speed of the profilometer to move from C_1 point to C_2 point to v. Then in a single scan, the line resolution on the Y_w axis R is expressed as:

$$R = \frac{s}{v} \times f \tag{2}$$

The profile point resolution of the profilometer m is determined by the performance of the sensor, then the networked point cloud set $\left\{A_{X_w Y_w Z_w}\right\}$:

$$\left\{A_{X_w Y_w Z_w}\right\} = \begin{bmatrix} A_{00Z_w} & \cdots & A_{0mZ_w} \\ \vdots & \ddots & \vdots \\ A_{R0Z_w} & \cdots & A_{RmZ_w} \end{bmatrix} \tag{3}$$

In the figure, Point A represents the three-dimensional information of any point in the measurement window, recorded as (X'_w, Y'_w, Z'_w), where the Point A in the world coordinate system has the actual three-dimensional information as:

$$A = \left(X'_w \frac{d}{m}, Y'_w \frac{s}{R}, Z'_w\right) \tag{4}$$

where d is determined by Formula (1) as the width of a single scan, and Z'_w is the height information measured by the laser profilometer. The measurement window width is l. To avoid the missed inspection, that is, each scan area needs to overlap, then the number of scans N_T needs to meet:

$$N_T > \frac{l}{d} \tag{5}$$

As shown in Figure 5, the profilometer moves from the initial position point C_1 to point C_n, resulting in N_T networked 3D point cloud images. After the complete scanning, the profilometer is returned to the origin.

3.1.2. Registration of 3D Point Cloud Mosaic

Multiple 3D point clouds were acquired under the 3D modeling method of complex terrain surface. Multiple point clouds were matched into a unified coordinate system through rotation dislocation and translation dislocation. The scanning viewpoints in this system were all in the same coordinate system, only related to the X-axis and Y-axis movement, i.e., being translated on the X-axis and reversed on the Y. The schematic diagram of point cloud registration is shown in Figure 6.

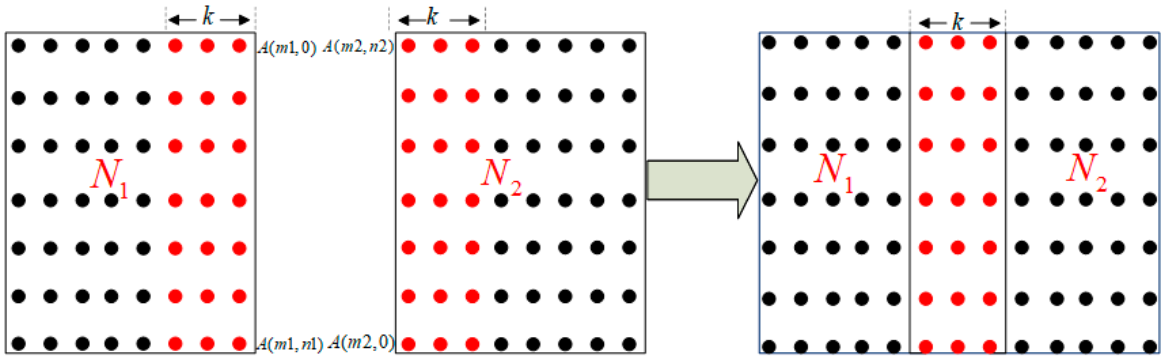

Figure 6. Schematic diagram of point cloud registration.

Looking at the trajectory of the profilometer in Figure 5, there is a reverse relationship between the two point cloud images of N_1 and N_2. The storage is in a sequential order, and they are opposite in space position. The point clouds need to rotate 180° for misalignment registration. Considering avoiding loss of sampled data points, there were k resampling units in the two point cloud images, and the stitched boundary point cloud data was obtained by means of averaging.

$$A(m,n) = \frac{A(m1,n1) + A(m2,n2)}{2} \tag{6}$$

where $A(m,n)$ is the point cloud data after registration, $A(m1,n1)$ is the data obtained by the first scanning, and $A(m2,n2)$ is the data obtained by second. After averaging, the original overlapping redundant data was substituted to get a complete 3D point cloud image.

3.1.3. Three-Dimensional Point Cloud Filtering

Due to errors caused by the measured terrain surface and the measurement system itself, the measured 3D point cloud may contain noises. These noises would cause the quality decreasing of the point cloud data, posing a great impact on the movement control of the probe behind. When it comes to denoising the point cloud, the proposed algorithms for ordered or partially ordered denoising means include Wiener filtering, Kalman filtering, smoothing filtering, median filtering, etc. [20]. For the impulse noise that occurs during the scanning process, the commonly used standard median filter algorithm can effectively filter out regardless of the filter output estimate that may differ from the real

information in the center of the filter window. As the filter window moves, this deviation will also participate in the calculation of the center point of other filtering windows, leading to the accumulation of errors. In this work, a center-weighted median filtering algorithm was used to filter out the impulse noise. The similarity between the point clouds in the filter window was taken in to assign the weight of each point to participate in the calculation. In this way, the deviation of the filtered output value from the real value was reduced, and the true depth information of the sampling point was better retained.

Using the 3×3 filter window, the first step is to use the similarity function to calculate the similarity between each point cloud in the window and the point cloud in the center of the window, and sort their sizes. Each pixel in the filter window was adaptively given a corresponding weight. Finally, perform weighted median filtering on the point cloud of the filter window center to obtain the output response of the window center. The three-dimensional networked point cloud may be projected in the two-dimensional space. In this background, the magnitude of similarity is reflected as the Euclidean distance between the center point cloud of the filter window and the other point clouds in the window. The closer the distance from the center point cloud of the filter window, the greater the similarity and the same to weight. The principle diagram of Euclidean distance weighted filtering is shown in Figure 7.

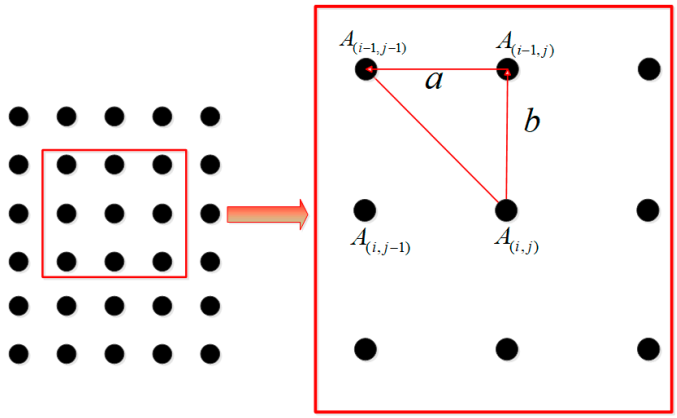

Figure 7. Schematic diagram of weighted median filtering principle.

We use the similarity function to calculate the similarity of each point cloud in the window. The similarity function uses the monotonically decreasing function $\varphi(x) = \frac{1}{1+x}$ in $[0, +\infty]$, where x is the distance between the point cloud and the center of the window. The similarity between the point $A_{(i-1,j-1)}$ and $A_{(i,j)}$ is defined as $S_{(i-1,j-1)}$:

$$S_{(i-1,j-1)} = \frac{1}{1 + \sqrt{a^2 + b^2}} \tag{7}$$

Then $S_{(i,j-1)=\frac{1}{1+a}}$, $S_{(i-1,j)=\frac{1}{1+b}}$. Similarly, the similarity between each point cloud in the filter window and the center point of the filter window. The distance a is related to the line resolution of the profilometer m, $a = \frac{c}{m}$, $b = \frac{S}{R}$, R are the scanning resolution of the profilometer in the Y_w axis direction, R see Equation (2). Let P_A be the sum of the similarities of the point clouds in the filter window except for the center point cloud, and then assign the weight of the point cloud in the window according to the similarity W:

$$P_A = \sum_{u=i-1}^{i+1} \sum_{v=j-1}^{j+1} S_{(u,v)}, (u \neq i, v \neq j) \tag{8}$$

$$W_{(u,v)} = \frac{S_{(u,v)}}{P_A} \tag{9}$$

$$A_{(i,j)} = \sum_{u=i-1}^{i+1} \sum_{v=j-1}^{j+1} W_{(u,v)} \times A_{(u,v)} \tag{10}$$

In Equation (8), P_A stands for that the Point Cloud A has the similarity between a point and Point Cloud A in the spatial neighborhood. u, v is the point coordinate position of the Point Cloud A area, excluding the Point Cloud A. The formula $W_{(u,v)}$ represents the filter weight of the Point Cloud A points in the spatial neighborhood, and finally, the value after A. The X axis and the Y axis of this system were different as far as the resolution is concerned, and the resolutions were higher. Additionally, the elevation information between adjacent point clouds had a high similarity. Each point in the traditional median filter window shared the same weight value. As a result, a large deviation occurred between the output response of the filter window and the true value. A deviation of this kind was easy to cause error transmission with the movement of the filter window. Comparatively, the median weighted filtering based on the Euclidean distance of the point cloud assigned the weight of the point cloud by the distance between the point clouds. The filter output obtained by this method may effectively reduce this deviation.

3.2. Motion Control Strategy of Surface Contamination Detector

The motion control of the probe requires terrain data as a control input. There are 36 channels in the array-type pollution detection unit. The 36 probe channels are respectively mapped in the measurement area to calculate the maximum depth value in each small area.

Ideally, the measurement area may be evenly divided into 36 parts, which, respectively, are mapped 36 measurement channels. Due to the mechanical assembly and mechanical processing, the probes were not arranged equidistantly or without gaps, and there was a large positional deviation. As shown in Figure 8.

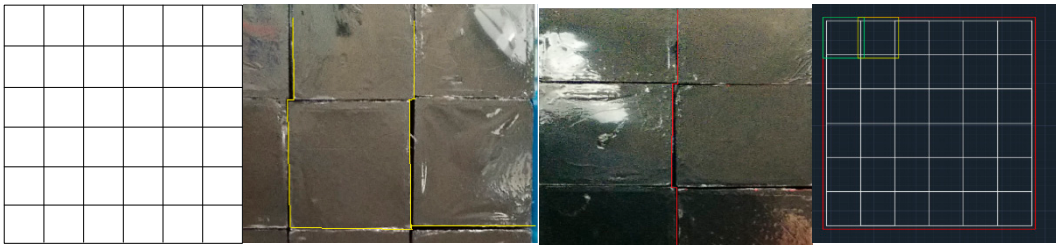

(**a**) (**b**) (**c**) (**d**)

Figure 8. (**a**) The segmentation model in an ideal state, and the terrain is evenly divided into 36 blocks. (**b**,**c**) The actual probe arrangement in a non-uniform way. Given the actual installation and arrangement of the probe, the ideal uniform cutting method still cannot be selected. The edge of the block needs to be blurred to be expanded on the basis of uniform cutting, as shown in (**d**).

The surface contamination detector moves under the control of high-precision stepping motor and screw drive. The communication works on the RS485 bus that a full-duplex communication, configured with a number of detector channels. To ensure communication efficiency and response speed, two groups of 485 buses were combined to communicate with 18 channel motors. In addition, a code disk was added to the stepper motor to achieve closed-loop control, and a brake device was engaged on the shaft to complete the motor self-locking function. The terrain information of each measurement was transmitted to the main control system, which distributed the supply of the stepper motor mapped to the terrain with the counter on the motor code wheel as control feedback. The block diagram of the motor control system is shown in Figure 9.

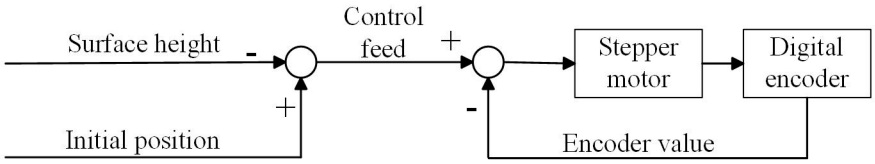

Figure 9. Schematic diagram of stepper motor control.

There are two inputs for motor control, one for the measured terrain height and the other for the initial position of the motor. By calculating the two inputs as the motor control feed, the motor code disc count value is read as control feedback to control the motor movement. Due to the mechanical installation errors of the detector, lead screw and motor, the initial position of each detector may be different from each other. The mechanical position of each channel detector should be calibrated and compensated for errors. The actual differences are seen in Figure 10.

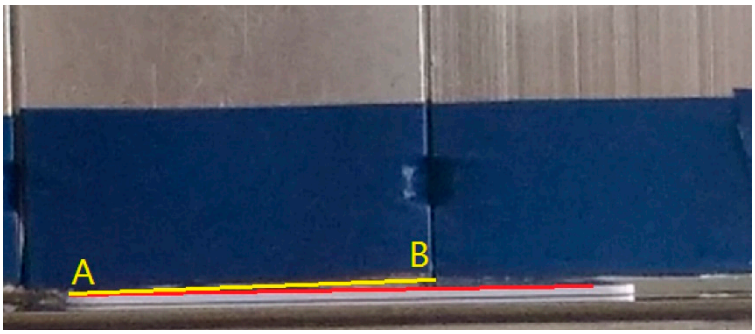

Figure 10. Schematic diagram of probe installation error.

The points A and B at the bottom of the probe are not in a uniform horizontal plane. The lowest, Point A of the probe position, is used as the reference position for channel control, and the horizontal position of A is recorded as the initial horizontal position of the detector as the motion control input of the detector. The driving motor was the STM11Q-3RE high-precision stepper motor produced by Shanghai MOONS Electric Ltd. The working DC voltage was 15–30 V in the RS-485 communication mode. The maximum output torque was 120 $mN \times m$. The torque curve of the motor is shown in Figure 11, where the dotted line is the torque curve of the motor under no load, and the solid line is the torque curve at full load.

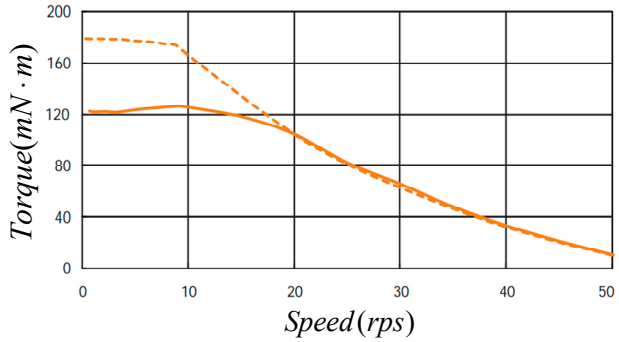

Figure 11. Torque curve of the drive motor.

3.3. Surface Pollution Array Detection Unit

The surface pollution detection unit is a device used to measure the radioactivity on the target surface. A semiconductor α and β particles detector was arranged to detect the target. The surface contamination detection subsystem consists of a front-end sensor measurement channel, a probe data

processing box and an industrial computer. Distributed in 6 × 6 array, a single channel is composed of a surface contamination detector, an adjustable screw and a stepper motor. The single channel is shown in Figure 12.

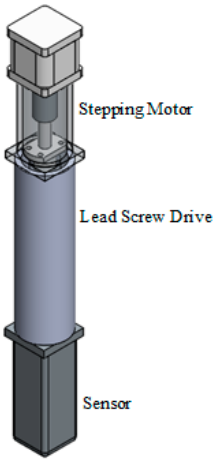

Figure 12. Diagram of single measurement channel.

The stepping motor was available to adjust the distance between the probe surface and the measured surface. The set distance was in a range of 1 mm to 5 mm, the counting time may be 1 s, 6 s, 10 s, 30 s and 60 s in several manual setting modes. Each channel and the digital communication controller were connected by a power line and a data line, which may simultaneously measure two kinds of particles: α, β. The digital communication controller sampled the data of the data probe and processes it into a digital signal. Via UART (Universal Asynchronous Receiver/Transmitter), this signal was then transmitted to the digital display platform that presents the data to the user.

The surface pollution array detection unit adopts α and β particles scintillator detectors. The scintillator detector is a kind of widely used radiation detector which uses the flash of radiation produced in certain substances for radiation detection. The incident radiation would get into the scintillator and loses energy in the scintillator, which could cause ionization and excitation of the scintillator atoms and generate visible light. The photon hits the photomultiplier tube through the light transmission process to produce photoelectrons. Finally, the electrons reach the anode and form a voltage pulse. Suppose M is the multiplication coefficient of the photomultiplier (PMT) tube, N is the number of photoelectrons generated by photons hitting the cathode, then the number of electrons collected at the output terminal is MN, and the corresponding pulse charge number is Q can be obtained by

$$Q = eMN \tag{11}$$

Then the voltage pulse V:

$$V = \frac{Q}{C} = \frac{neME}{C} \tag{12}$$

where C is the output capacitance, $n = N/E$ is the number of photoelectrons produced per unit energy of the incident particle. e is the amount of charge a unit photoelectron has, and E is the incident particle energy.

The α and β particle detectors used in the proposed approach select a composite scintillator composed of ZnS (Ag) scintillators and plastic scintillators. The composite scintillator is uniformly coated with ZnS (Ag) on a thin plastic scintillator. The ZnS (Ag) crystal can absorb all incident α particles, and the β particles with lower energy, which can pass through the ZnS (Ag) crystal. Then, the β particles will enter the plastic scintillator and will be recorded. In addition, this composite scintillator can be made into a variety of sizes and shapes, which is suitable for the surface pollution detection unit designed herein. The count rate is obtained by the statistical number of voltage pulses

to characterize the radioactive activity of the radioactive source. The detector's count rate for the standard planar source divided by the standard planar source unit area activity is the surface activity response of the pollution instrument $(s^{-1}Bq^{-1}cm^2)$.

$$R_a = \frac{\overline{N} - N_b}{A_s} \tag{13}$$

where R_a is the surface activity response of the surface contamination detector for α and β. $\overline{N}$ is the counting rate of the detector to the standard source, N_b is the counting rate of the detector to the standard source. A_s is the activity per unit area of the standard plane source. In practical applications, the reference value of the α and β standard planar sources is the surface emissivity, and the surface source emissivity expressed as q is related to the radioactivity through the planar source efficiency ε.

$$A = \frac{q}{\varepsilon} \tag{14}$$

where A is the radioactivity of the source, q is the surface emissivity of the planar source. Following this, we divide the radioactivity of the planar source by the surface area of the planar source to get A_s. Normally for α-plane sources, $\varepsilon(\alpha) = 0.51$, $\varepsilon(\beta) = 0.62$. Relatively inherent errors are usually used to describe the accuracy of system measurements.

4. System Implementation and Experimental Verification

This section describes the specific implementation of the proposed method and discusses the experiment of related indicators. As the control foundation of the system, the experimental platform must be reasonable and reliable. The experimental platform mainly includes the overall structure, the motion platform of laser profilometer, the control platform for detector motion and the computer processing platform. We designed three experiments to verify the effectiveness of the system. The first experiment tested the time consumption and scanning accuracy of the system, and analyzed the effectiveness of the surface profile measurement subsystem; the second experiment separately tested the control accuracy of 6×6 channels, plus the reliability of our method in different scenarios; the third experiment aimed at the activity response of the surface contamination detection system to a standard planar source, testing the effect of different measurement heights on the surface contamination detection error, qualitatively analyzing the feasibility of the system.

4.1. System Implementation

The overall mechanical structure of the system is like a hand-push box, equipped with four universal wheels as the center of gravity support, featuring high maneuverability. The mechanical structure of the system includes a laser profilometer motion platform, which is a two-dimensional LLT-2900-100 high-speed profilometer produced by Germany-based Micro-Epsilon. It operates with a semiconductor laser having a wavelength of 658 nm (visible/red). When the measured object is a complex surface with high transmittance, such as glass, the depth/geometric profiling will be affected. The measurement scenes involved in this paper are mainly metal surface and concrete surface, in generally the system will not be used in the case that reflected light is blocked obviously, so the profilometer is chosen to meet the requirements of the system. The motion platform consists of an *X*-axis motion platform, a *Y*-axis rectangular coordinate motion platform and a cable protection towline. The combination of two displacement platforms enforces the complete movement of the profilometer in the horizontal plane of the detection area. The control platform for 6×6-channel detectors motion contains a total of 36 detection channels that can be moved simultaneously or separately. Each of these channel packages incorporates MOONS's STM11-3RE series integrated stepper motors and the custom couplings and radiation detectors, aiming at high-precision control. The user operation platform is

composed of industrial computers and located in the most mechanical structure of the system upper layer. The mechanical structure of the system is shown in Figure 13.

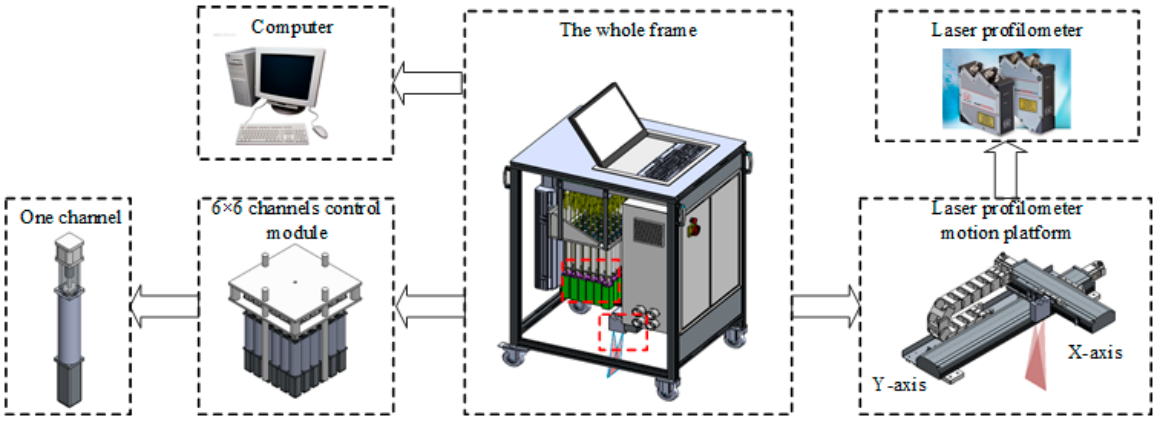

Figure 13. Mechanical structure of the system.

According to the mechanical structure of the system, the corresponding physical platform was built, as shown in Figure 14. *M_Z* is the *Z*-axis ready to control the up and down movement of the 6 × 6 array detection channel platform, *M_X* is the *X*-axis and *M_Y* is the *Y*-axis, and *M_S* is responsible for the single-channel detector movement. The overall support frame was built with anodized aluminum profiles in conformity with the European Commission's standard; *M_X* and *M_Y* worked with the TL170 single-arm motion platform. This is a semi-closed screw series with the motor power up to 400 W and the repeat accuracy ±0.02 mm; *M_Z* used the M2DV-4D52R servo motor as the drive, and the mechanical layout of the detector was organized in a 6 × 6 array. As to the experimental platform, the overall dimensions are L900 × W800 × 1300 mm^3, the *X*-axis travel is 400 mm, the *Y*-axis travel is up to 350 mm, the *Z*-axis travel is 450 mm, and the surface contamination detector travels up and down approximately 110 mm.

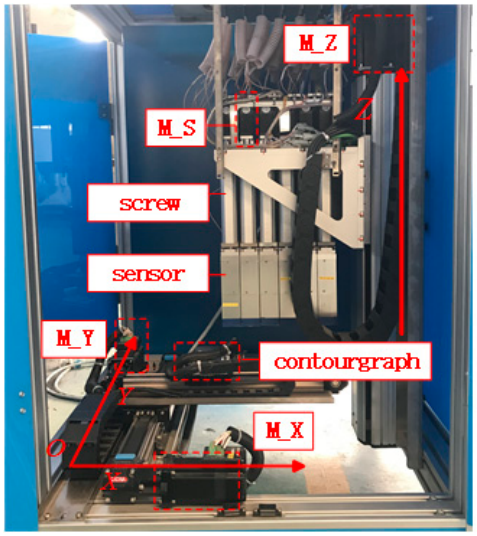

Figure 14. Schematic diagram of the system.

The software implementation part operated on Windows 10 as its system environment, being equipped with Visual Studio 2015 and Qt5.8. The software design part mainly includes acquisition and processing of point cloud data, motion control of the 6 × 6 detection channel, data reading and storage

of surface pollution detector as well as terrain surface data and visualization of pollution detector data. The software flow chart is shown in Figure 15.

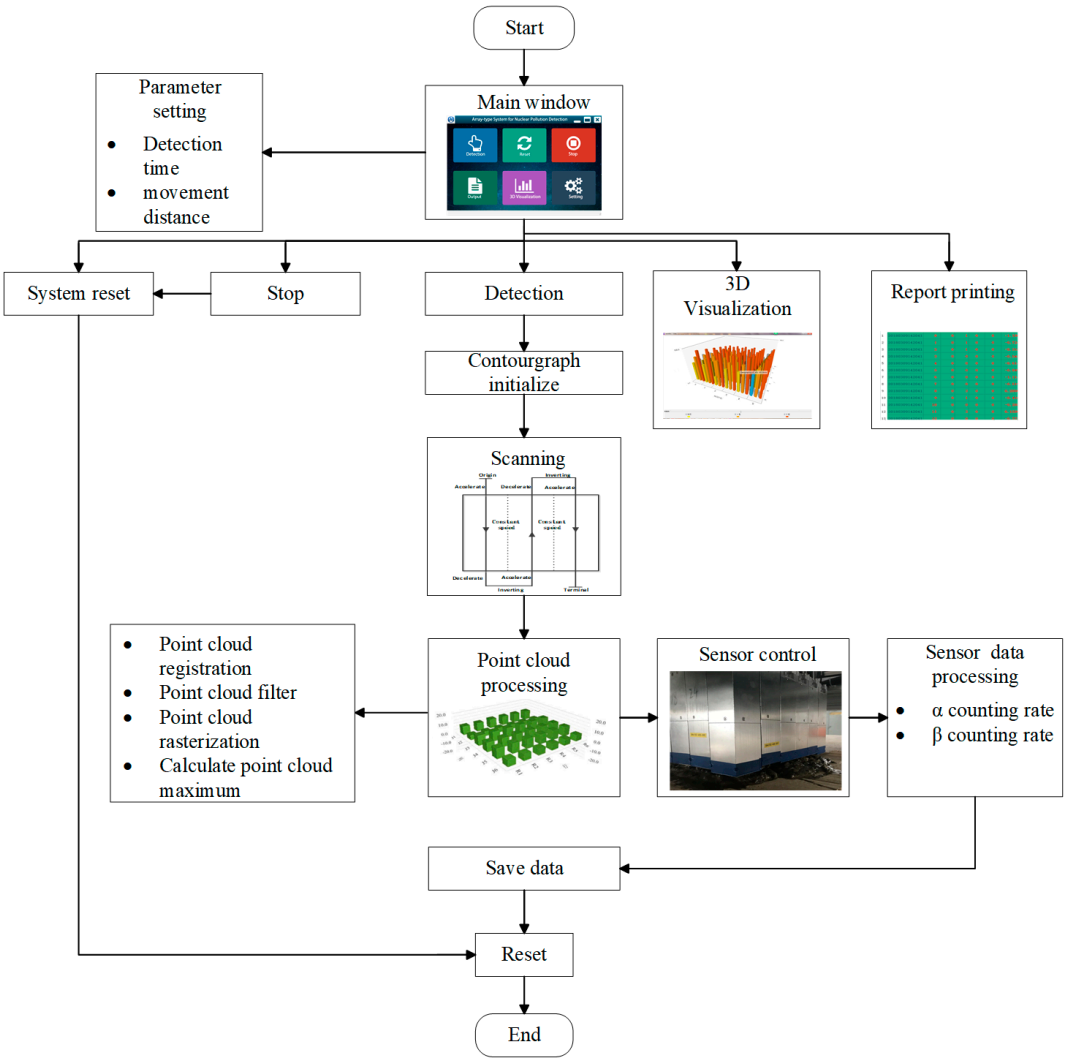

Figure 15. Flow chart of detection method for nuclear surface contamination.

After the program starts, the initial position of the horizontal level of the detection channel will be self-checked. If the self-checking fails, it will prompt the coordinates of the abnormal channel position, and then perform the reset operation. After the self-test passes, the profilometer is initialized, and the point cloud data is collected and processed. The maximum height of the terrain corresponding to the 6×6 channels is calculated, and then converted to the motor feed. Subsequently, the pollution detector is controlled to move downwards. After moving to a given position, the surface α and β particles are collected, the detector data is read and stored in the database, and finally the terrain surface data and the detector measurement data are visualized in 3D and the data report is printed out to complete the above process prior to resetting the system.

Figure 16 is the effect diagram of the software interface, where (a) is the main interface of the system, including six buttons for such functions as detection, reset, and stop, etc. The stop button has the highest priority and it interrupts the system process after the system is found to be abnormal, protecting the system from being damaged; (b) is a 3D histogram of the location of each detection channel and its corresponding surface terrain height and pollution meter detection value; (c) shows the interface as a visual interactive interface for historical data query, querying historical data at each time period, available for the printout of data reports.

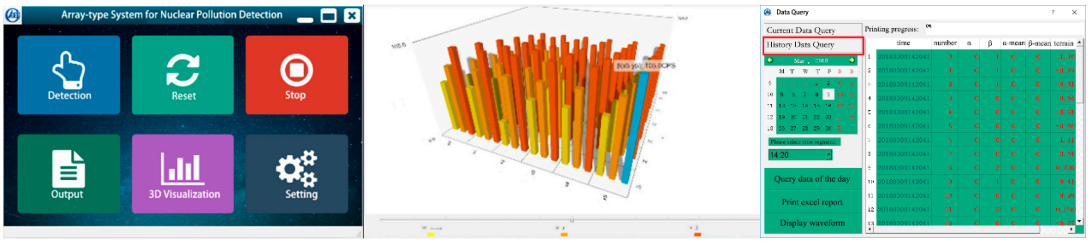

(**a**) (**b**) (**c**)

Figure 16. The system's human-computer interface. (**a**) The main interface. (**b**) The data visualization window. (**c**) The data query window.

4.2. Experimental Verification

4.2.1. Evaluation of Runtime Overhead Test of Array Detection Method

The authors tested the system running time overhead and surface topography scanning accuracy. According to the requirements of the system time index, the movement speed of each degree of freedom needs to be specially set. For too low a speed, the overhead may increase. For a higher one, there may be a step loss under load, and so is the control accuracy. In the worst case, the inertial motion carrier may exceed the limit switch. *M_X* axis and *M_Y* axis are driven by belt, *M_Z* axis and *M_S* axis by screw. See the transmission device parameters of the experimental platform are shown in Table 1.

Table 1. The parameters of each axis on displacement platform.

Displacement Platform	Motor	Helical Pitch (mm)	Stroke (mm)
M_X	STM24SF-3RN	95	400
M_Y	STM24SF-3RN	75	350
M_Z	M2DV-4D52R	5	450
M_S	STM11-3RE	2	110

When testing the time overhead of the analysis system, we divided the movement of the profilometer into 7 segments (*t*1 to *t*7), and the downward movement of the 6 × 6 array channel was divided into *t*8 to *t*9, as shown in Figure 17, where O is the initial position.

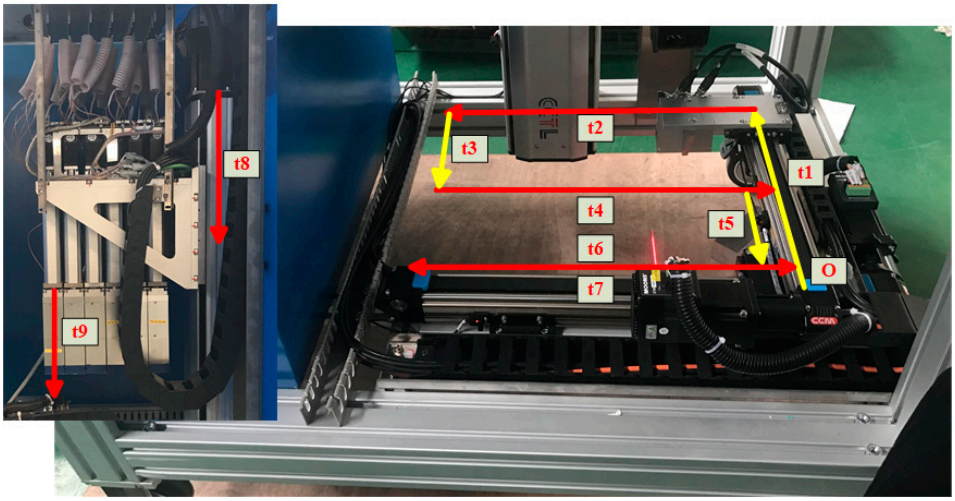

Figure 17. Schematic diagram of movement path of the *X*-axis and *Y*-axis motion platform.

The movement time of each process was tested separately and compared with the theoretical calculation value, see Table 2. *t*8 is the descent time of the *Z*-axis with the 6 × 6 array platform,

the descent distance is 15 cm; *t*9 is the descent movement time of a single measurement channel. If 36 channels are moving at the same time, the maximum descent range is 10 cm according to the index requirements, so the theoretical value of the maximum movement time is 5 s.

Table 2. Test on time consumption.

Number	t1	t2	t3	t4	t5	t6	t7	t8	t9	all
Theoretical value (s)	3.15	2.46	1.57	2.46	1.57	2.46	2.46	3.0	5.0	24.13
Test value (s)	3.24	2.56	1.79	2.54	1.78	2.55	2.67	3.70	5.30	26.13
Error	0.09	0.10	0.22	0.08	0.21	0.09	0.21	0.7	0.3	2.0

From Table 2, the actual test time consumption increased compared to the theoretical value. The theoretical total motion time is 24.13 s and the actual measured time is 26.13 s. Both the theoretical and actual measured values meet the system time requirements. The reasons why the test result was higher than the theoretical runtime are as follows:

1. Two groups of 485 communication method was adopted, each way mounted with 18 devices, the communication latency was 200 ms.
2. Unlike the value calculated theoretically for no-load, the motor was loaded during the actual test. The speed was lower than the theory under the load with the same parameters.
3. In the comparison table, it is particularly found that the difference between the test value and the theoretical value in *t*8 is the largest, and the storage and calculation of the three-dimensional point cloud is included in this movement time period.

The motion parameters of the profilometer may also affect the sampling rate of the topography of the measured surface. The resolution of a single contour of the profilometer line is 320, the length of the line is 112 mm, and the operating frequency is 270 Hz. The sampling platforms are *t*2, *t*4 and *t*6. Table 3 is the resolution we actually measured.

Table 3. The scanning resolution of surface contour detection unit.

Number	Length and Width(mm)	Test-Resolution (L × W)	Theoretical-Resolution
t2	240 × 78.6	694 × 225	691 × 225
t4	240 × 77.7	690 × 222	686 × 222
t6	240 × 83.7	693 × 239	689 × 239

From Table 3, the actual value of the *X*-axis resolution is consistent with the theoretical value, which is determined by the built-in parameters of the profilometer. The theoretical resolution of the *Y*-axis can be calculated by Equation (2), which is not much different from the measured value. The slight difference is due to a slight fluctuation in the operating frequency of the profilometer, and there is a small error between the measured value and the theoretical value due to the accumulation of time. To facilitate the registration of the point cloud, we unified the resolution on the *Y*-axis. It would be more appropriate to measure the *Y*-axis resolution to 689 through 100 experiments, so the surface point cloud resolution is 689 × 686 (L × W), and the scanning accuracy is 0.35 × 0.35 mm^2.

4.2.2. Evaluation of Motion Control Effect of Detector

A standard horizontal platform is selected as the measurement object, the system is placed on the horizontal platform in parallel. The system scans the platform, then controls the detector to descend, and sets the distance between the detector horizontal plane and the horizontal platform at 1 mm. Some standard measurement tools are adopted to measure the distance between the detector and the ground, as shown in Figure 18.

(**a**) (**b**)

Figure 18. Measurement experiment tools and effect diagram. (**a**) The measuring tools. (**b**) The effect diagram.

Figure 18a is a standard thickness circular gasket verified by a vernier caliper, ranging from 0.2 mm to 1.5 mm. After the end of detector descending, the standard tool above was used to measure the detector motion control error. The error test of motion control was carried out on 36 channels, each for 50 times. The test statistical results are shown in Figure 19.

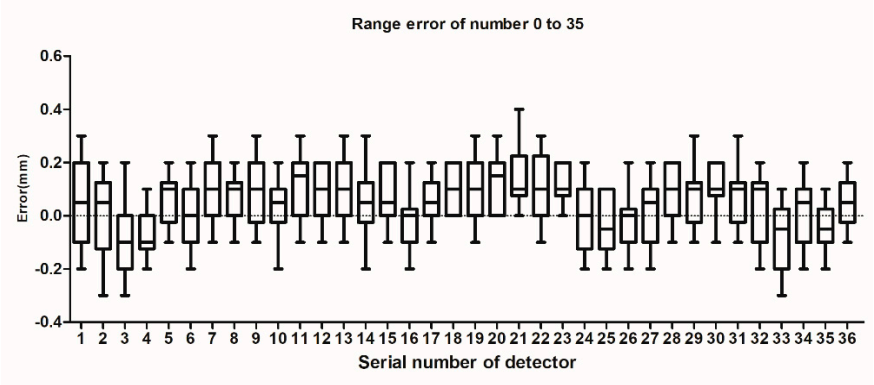

Figure 19. Box diagram of motion control error of 36-channel detector.

The test results are displayed in the paper in the form of a box chart, describing the distribution of error data for each channel. In Figure 19, the error box chart for channels 0 to 35. The motion control errors of all detection channels were basically distributed from −0.2 mm to +0.2 mm, with the maximum error of 0.4 mm.

4.2.3. Evaluation of Detection Efficiency for Surface Pollution

The surface activity response is the most important parameter to measure the performance of the surface pollution meters with α and β particles. During the measurement process, accurate control of distance is critical to the accuracy of surface activity response magnitude. This experiment was designed to verify the performance of the surface contamination detection subsystem. The standard plane sources of α particle and β particle were used to give a qualitative and quantitative analysis of the influence of the distance on the surface activity response of the surface contamination detectors for α and β particles. Figure 20 is the physical map of the surface pollution detection system. In addition to a 36-channel pollution detector, the system is also equipped with a digital communication controller dedicated to storing and uploading the measurement data of the detector.

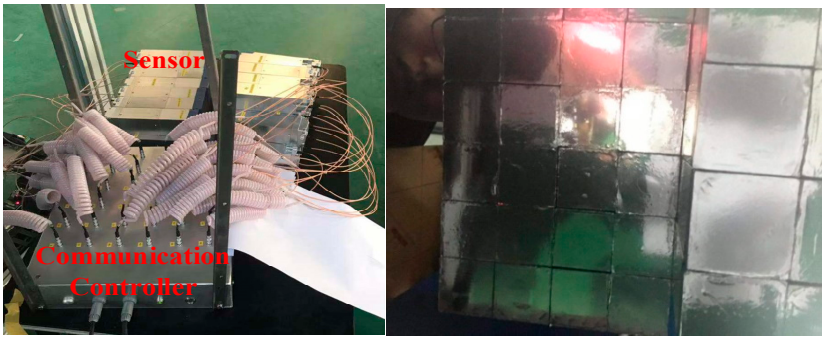

(**a**) (**b**)

Figure 20. Physical diagram of probe surface and digital communication controller. (**a**) The detector and communication controller. (**b**) The schematic diagram of the detector surface.

The standard plane source of α particle used in the experiment was Am-241. The rest data included an active area 150 cm^2, surface activity 14.58 Bq cm^2, Source of β particle was T1-204, including an active area 150 cm^2, surface activity 11.69 Bq cm^2. The reading value of the detector is the count rate (s^{-1}), the area of the detection surface is 4 × 4 cm. It is believed that each point within plane sources of α particle and β particle shared the same surface activity, and 36 channels may be detected at the same height at the same time. Using the upper left corner of the detector as the starting point, the resolution number was 0 to 35, and the surface activity response of each channel was calculated separately. Then adjust the distance between the detection plane of the detector and the plane source, continue to test the surface activity response of each channel, adjust the distance to 3–7 mm. Meanwhile, the test value at 3 mm was agreed as baseline, with the detection efficiency here set to 100%. Next, the two sources (α, β) were separately detected by the surface pollution detection system. The experiments were performed at different distances, and the count values of 36 channels were averaged.

In this paper, when the detector measures α particle, the distance adjustment range is 3–5 mm. For β particle, the distance adjustment is 8–12 mm. The activity response of the radioactive source is measured at different distances, and the measurement efficiency of the instrument at different distances is obtained. According to Tables 4 and 5, it can be concluded that the smaller the distance between the detector and the source, the higher the surface activity response value and the higher the detection efficiency. The distance has a great influence on the detection result. In actual use, the accuracy of the distance needs to be strictly maintained. The system can meet the requirements of precise distance control.

Table 4. The source of α particle surface activity response test at difference distance.

Distance (mm)	Surface Activity Response ($s^{-1}Bq^{-1}cm^2$)	Detection Efficiency (%)
3	6.9	100
4	6.5	94.2
5	6.1	88.4
6	5.7	82.6
7	5.3	76.8

Table 5. The source of β particle surface activity response test at difference distance.

Distance (mm)	Surface Activity Response ($s^{-1}Bq^{-1}cm^2$)	Detection Efficiency (%)
8	7.2	100
9	6.9	95.8
10	6.6	91.6
11	6.3	87.5
12	6.0	83.3

5. Performance of System and Discussion

Experiments on the experimental platform showed that it could automatically measure complex surfaces with a height difference of ±5 cm, being able to better restore the three-dimensional information of the terrain surface. The scanning accuracy was as good as 0.35 mm, and the surface height measurement accuracy was 12 μm, along with the single measurement area up to 240 × 240 mm^2. The runtime of completing a surface 3D information measurement and motion control was 26.13 s, and the maximum control error of the detector movement was 0.4 mm. Tests were also separately performed on different lighting, surface materials and venues. Experiments have shown that the system was able to respond to some basic environmental changes for motion control of the pollution detector. To verify the feasibility of the detection of surface nuclear pollution intensity, tests were also done on condition of standard planar sources (α, β). The effects of different detection distances on the detection efficiency and maximum relative error of the system were analyzed accordingly.

In complex surface environments, our method has obvious advantages. Compared with manual detection [6], our method has the characteristics of large detection range and high efficiency. For a mobile robot [10], our method is less affected by the ground environment. For a flying robot [17], our method has higher efficiency and precision.

In the motion control of the profilometer, the acceleration/deceleration control algorithm based on trapezoid-curve is adopted to ensure that the profilometer is in a uniform motion state during the scanning process. Further, the motion scanning scheme of an 'S' shaped curve is applied to ensure the integrity of the scanning area, which can reduce the operating time. Besides, two groups of 485 communication method and multi-threading are utilized to improve the real-time response time of the system.

The advantages of resilient detection are manifested in the following two aspects. Firstly, by controlling 36 stepping motors descending to different heights, the proposed array-type system can detect the pollutions of complex nuclear surfaces, which is difficult for conventional devices to achieve. Secondly, the *XY* two-axis motion platform and 'S' type scanning scheme are utilized in the horizontal direction, which can detect a larger range.

However, there are still some places that need to be improved. When testing the runtime overhead, the system was found to run over more time for processing the point cloud, and needs to be further optimized in this regard. Limited by the range of the profilometer, the effective range is trapezoidal. The higher the height, the smaller the horizontal range. If the height difference of the measured surface exceeds ±5 cm, it may cause a measurement dead zone within the set scanning area range. The restoration of the three-dimensional information on the surface could therefore be harmed, resulting in abnormal detection.

6. Conclusions

In this paper, an array system applied to complex surfaces was constructed for nuclear pollution detection. The measurement model of the two-dimensional laser profilometer was also analyzed. An 'S' scanning mode of profilometer, combined with the laser profilometer and the motion parameters, was used to obtain the three-dimensional terrain information. Due to the limited working area of a single laser profilometer, the system measured the target area in blocks. By the way of point cloud

registration, complete point cloud data was obtained. Besides, Euclidean distance median filtering was introduced to solve the impulse noise problem of point cloud. On the surface contour, the rasterized 3D point cloud data was mapped to the lower plane of the pollution detector. Due to the position error caused by the machinery and installation, the edges must be blurred when rasterized. After the rasterization, the maximum value of the point cloud and the initial position of the probe were calculated as the motor closed-loop control input, with the code wheel count of the stepper motor as feedback. Likewise, due to mechanical and installation errors, the initial position of the probe was compensated to guarantee more robustness of the system control. Finally, considering the friendly human-computer interaction, a visual interface with data visual output was also included on the experimental platform. The experiment proved that the proposed methodology may effectively obtain three-dimensional terrain information. The scanning accuracy was 0.35 mm in X-axis and Y-axis, and the measuring accuracy was 12 μm in Z-axis. It also realized control over the movement of the pollution detector accurately, regardless of the maximum control error 0.4 mm. The single measurement area even got up to 240 × 240 cm^2, and the time for single complete detection was 26.13 s. As a bonus, this new system completed the detection of α and β particles. For future work, we plan to optimize method of point cloud processing for improving the detecting efficiency.

Author Contributions: H.C. conceived and designed the system solutions, and wrote the paper; Z.C. performed the experiments; Y.S. analyzed the data and summarized the conclusions; X.Z. and J.L. provided some useful suggestions, performed overall revision and supervision for these experiments and paper, and also performed project administration and funding acquisition. All authors have read and agreed to the published version of the manuscript.

Funding: This work is supported by National Natural Science Foundation (NSFC) of China under Grant No.61601382, Sichuan Provincial Science and Technology Support Project No.2019YJ0325, the Doctoral Fund of Southwest University of Science and Technology No.16zx7148, No.19zx7123, Longshan academic talent research supporting program of SWUST No.18LZX632 and the Fund of Robot Technology Used for Special Environment Key Laboratory of Sichuan Province No.13zxtk08.

Conflicts of Interest: The authors declare no conflict of interest.

References

1. El-Gammal, W.; Darweesh, M.; Shawky, S. Investigation of a dynamic measurement methodology for fast detection of gross defects in regularly distributed nuclear material samples. *Heliyon* **2019**, *5*, e02110. [CrossRef]
2. Lin, T.-H.; Wu, S.-C. Sensor fault detection, isolation and reconstruction in nuclear power plants. *Ann. Nucl. Energy* **2019**, *126*, 398–409. [CrossRef]
3. Musolino, S.V.; Buddemeier, B.; Finfrock, C.; Gomera, J.; Klemic, G.; Moskowitz, J.; Roberts, T.; Schaefer, L. Evaluation of Repurposing Archetypal Preventive Radiological. *Health Phys.* **2019**, *116*, 4–17. [CrossRef]
4. Yamamoto, H.; Hayashi, K.; Scherb, H. Association between the detection rate of thyroid cancer and the external radiation dose-rate after the nuclear power plant accidents in Fukushima, Japan. *Medicine* **2019**, *98*, 27–36. [CrossRef] [PubMed]
5. Tran, L.T.; Prokopovich, D.A.; Lerch, M.L.; Petasecca, M.; Siegele, R.; Reinhard, M.I.; Perevertaylo, V.; Rosenfeld, A.B. Development of a large-area silicon α-particle detector. *Appl. Radiat. Isot.* **2014**, *92*, 96–101. [CrossRef]
6. Terasaki, K.; Fujibuchi, T.; Murazaki, H. Evaluation of basic characteristics of a semiconductor detector for personal radiation dose monitoring. *Radiol. Phys. Technol.* **2017**, *10*, 189–194. [CrossRef]
7. Liu, L.-Y.; Wang, L.; Jin, P.; Liu, J.-L.; Zhang, X.-P.; Chen, L.; Zhang, J.-F.; Ouyang, X.-P.; Liu, A.; Huang, R.-H. The Fabrication and Characterization of Ni/4H-SiC Schottky Diode Radiation Detectors with a Sensitive Area of up to 4 cm2. *Sensors* **2017**, *17*, 2334–2351. [CrossRef] [PubMed]
8. Cester, D.; Lunardon, M.; Stevanato, L.; Viesti, G.; Chandra, R.; Davatz, G.; Friederich, H.; Gendotti, U.; Murer, D.; Iwanowska-Hanke, J. Commissioning and field tests of a van-mounted system for the detection of radioactive sources and special nuclear material. *IEEE Trans. Nucl. Sci.* **2016**, *63*, 1314–1322. [CrossRef]

9. Ryzhikov, V.; Gal'chinetski, L.; Galkin, S.; Danshin, E.; Kvitnitskaya, V.; Silin, V.; Chernikov, V. Combined detectors based on ZnSe (Te), CsI (Tl) and Si-PIN-PD for separate detection of alpha, beta and gamma radiation. *IEEE Trans. Nucl. Sci.* **2000**, *47*, 1979–1981. [CrossRef]
10. Shen, H.; Zhu, W.; Dong, Q.; Chen, F.; Yan, S.; Han, Y. Development of the tele-control robot for nuclear detection in intense radiation environment. *Nucl. Electron. Detect. Technol.* **2015**, *35*, 74–78.
11. Kim, D.; Woo, H.; Ji, Y.; Tamura, Y.; Yamashita, A.; Asama, H. 3D radiation imaging using mobile robot equipped with radiation detector. In Proceedings of the 2017 IEEE/SICE International Symposium on System Integration (SII), Taipei, Taiwan, 11–14 December 2017; pp. 444–449.
12. Ducros, C.; Hauser, G.; Mahjoubi, N.; Girones, P.; Boisset, L.; Sorin, A.; Jonquet, E.; Falciola, J.M.; Benhamou, A. RICA: A tracked robot for sampling and radiological characterization in the nuclear field. *J. Field Rob.* **2017**, *34*, 583–599. [CrossRef]
13. Boudergui, K.; Carrel, F.; Domenech, T.; Guenard, N.; Poli, J.-P.; Ravet, A.; Schoepff, V.; Woo, R. Development of a drone equipped with optimized sensors for nuclear and radiological risk characterization. In Proceedings of the 2011 2nd IEEE International Conference on Advancements in Nuclear Instrumentation, Measurement Methods and Their Applications, Ghent, Belgium, 6–9 June 2011; pp. 1–9.
14. Martin, P.; Payton, O.; Fardoulis, J.; Richards, D.; Scott, T. The use of unmanned aerial systems for the mapping of legacy uranium mines. *J. Environ. Radioact.* **2015**, *143*, 135–140. [CrossRef] [PubMed]
15. Pöllänen, R.; Toivonen, H.; Peräjärvi, K.; Karhunen, T.; Ilander, T.; Lehtinen, J.; Rintala, K.; Katajainen, T.; Niemelä, J.; Juusela, M. Radiation surveillance using an unmanned aerial vehicle. *Appl. Radiat. Isot.* **2009**, *67*, 340–344. [CrossRef] [PubMed]
16. Kurvinen, K.; Smolander, P.; Pöllänen, R.; Kuukankorpi, S.; Kettunen, M.; Lyytinen, J. Design of a radiation surveillance unit for an unmanned aerial vehicle. *J. Environ. Radioact.* **2005**, *81*, 1–10. [CrossRef] [PubMed]
17. Towler, J.; Krawiec, B.; Kochersberger, K. Radiation mapping in post-disaster environments using an autonomous helicopter. *Remote Sens.* **2012**, *4*, 1995–2015. [CrossRef]
18. Cai, C.; Carter, B.; Srivastava, M.; Tsung, J.; Vahedi-Faridi, J.; Wiley, C. Designing a radiation sensing UAV system. In Proceedings of the 2016 IEEE Systems and Information Engineering Design Symposium (SIEDS), Charlottesville, VA, USA, 29 April 2016; pp. 165–169.
19. Micconi, G.; Aleotti, J.; Caselli, S. Evaluation of a haptic interface for UAV teleoperation in detection of radiation sources. In Proceedings of the 2016 18th Mediterranean Electrotechnical Conference (MELECON), Lemesos, Cyprus, 18–20 April 2016; pp. 1–6.
20. Wan, H.; Shi, F.; Liu, Q.; Li, S.; Zhen, G. Study on the application of point cloud denoising in Gobi desert surface. *IOP Conf. Ser. Earth Environ. Sci.* **2018**, *189*, 022011.